Physics in Medicine & Biology



# The adaptation and investigation of cone-beam CT reconstruction algorithms for horizontal rotation fixed-gantry scans of rabbits

To cite this article before publication: Mark Gardner *et al* 2021 *Phys. Med. Biol.* in press https://doi.org/10.1088/1361-6560/abf9dd

# The adaptation and investigation of cone-beam CT reconstruction algorithms for horizontal rotation fixed-gantry scans of rabbits

Mark Gardner[1], Owen Dillon[1], Chun-Chien Shieh[1,2], Ricky O'Brien[1], Emily Debrot[1], Jeffrey Barber[3], Verity Ahern[3], Peter Bennett[4], Soo-Min Heng[5], Stéphanie Corde[5], Michael Jackson[5], Paul Keall[1]

Affiliations:

1. ACRF Image X Institute, The University of Sydney, Eveleigh, NSW 2015, Australia
2. Sydney Neuroimaging Analysis Centre, Camperdown, NSW 2050, Australia
3. Western Sydney Local Health District, Blacktown, NSW 2148, Australia
4. Faculty of Science, The University of Sydney, Camperdown, NSW 2006, Australia
5. Nelune Comprehensive Cancer Centre, Randwick, NSW 2031, Australia

Email: mark.gardner@sydney.edu.au

Keywords: CBCT, image reconstruction, motion compensation, animal study, radiotherapy

## Abstract

Fixed-gantry radiation therapy has been proposed as a low-cost alternative to the conventional rotating-gantry radiation therapy, that may help meet the rising global treatment demand. Fixed-gantry systems require gravitational motion compensated reconstruction algorithms to produce cone-beam CT (CBCT) images of sufficient quality for image guidance. The aim of this work was to adapt and investigate five CBCT reconstruction algorithms for fixed-gantry cone-beam CT images.

The five algorithms investigated were Feldkamp-Davis-Kress (FDK), prior image constrained compressed sensing (PICCS), gravitational motion compensated FDK (GMCFDK), motion compensated PICCS (MCPICCS) (a novel CBCT reconstruction algorithm) and simultaneous motion estimation and iterative reconstruction (SMEIR). Fixed-gantry and rotating-gantry CBCT scans were acquired of 3 rabbits, with the rotating-gantry scans used as a reference. Projections were sorted into rotation bins, based on the angle of rotation of the rabbit during image acquisition. The algorithms were compared using the structural similarity index measure root-mean-square error, and reconstruction time.

Evaluation of the reconstructed volumes showed that, when compared with the reference rotating-gantry volume, the conventional FDK algorithm did not accurately reconstruct fixed-gantry CBCT scans. Whilst the PICCS reconstruction algorithm reduced some motion artefacts, the motion estimation reconstruction methods (GMCFDK, MCPICCS and SMEIR) were able to greatly reduce the effect of motion artefacts on the reconstructed volumes. This finding was verified quantitatively, with GMCFDK, MCPICCS and SMEIR reconstructions having RMSE 17-19% lower and SSIM 1% higher than a conventional FDK. However, all motion compensated fixed-gantry CBCT reconstructions had a 56-61% higher RMSE and 1.5% lower SSIM than FDK reconstructions of conventional rotating-gantry CBCT scans.

The results show that motion compensation is required to reduce motion artefacts for fixed-gantry CBCT reconstructions. This paper further demonstrates the feasibility of fixed-gantry CBCT scans,

and the ability of CBCT reconstruction algorithms to compensate for motion due to horizontal rotation.

## 1. Introduction

There is a rising global demand for radiation therapy systems, with an additional 13000 devices needed by 2035, requiring $96.8 billion of investment (Atun *et al.*, 2015). The unmet need is high in low- and middle-income countries and also in rural areas in high income countries such as Australia, USA and Canada (Atun *et al.*, 2015). Fixed-beam radiation therapy devices are potentially a low-cost and compact alternative to conventional radiation therapy devices (Eslick and Keall, 2015). In conventional radiation therapy devices, the gantry of the linear accelerator (linac), which weighs several tonnes, is rotated around the patient to precise angles to ensure accurate radiation dose distribution. However, in a fixed-gantry radiation therapy setup, the gantry is kept stationary and the patient is rotated. By rotating the patient instead of the gantry, there is a reduction in device costs and complexity, which could reduce the frequency in which maintenance is needed. Additionally, since the treatment beam is fixed, the shielding requirements for the bunker containing the linac are reduced, leading to a smaller room footprint further decreasing the cost (Eslick and Keall, 2015). Hence fixed-beam radiation therapy systems may help meet the global demand for radiation therapy.

Although vertical patient rotation, with a patient sitting or standing, may be more comfortable for some patients, horizontal patient rotation has several advantages over vertical patient rotation. First, for radiation therapy the treatment plans are developed on pre-treatment CT scans of the patient lying down. This means treatment plans would have to be adapted to match the changed anatomy of a patient standing up or sitting down. Yang et al. reported significant changes in lung volume between participants sitting upright and lying down (Yang *et al.*, 2014). Second, for some cancer patients it may be difficult to remain stationary during treatment whilst in a standing or a sitting position. Third, for a fixed-gantry horizontal rotation design, the treatment beam can be directed towards the ground, reducing shielding requirements for the treatment bunker, reducing costs. Previous studies have shown that radiotherapy patients will tolerate horizontal rotation (Whelan *et al.*, 2018; Buckley *et al.*, 2021). Currently, a clinical trial is underway to evaluate patient experiences while using a previously developed prototype patient rotation system (Liu *et al.*, 2019), with preliminary results suggesting patients tolerate rotation (Debrot *et al.*, 2020).

Outside of low-cost radiation therapy devices, fixed-beam radiation therapy setups also have other applications including proton therapy (Devicienti *et al.*, 2010) and MRI-linacs (Buckley, Dong and Liney, 2020) where there are challenges in rotating the gantry around the patient. This means that developments in fixed-beam radiation therapy could also be applicable to other fields.

Cone-beam computed tomography (CBCT) is routinely used in radiation therapy to assist in verifying the tumour position and to account for interfraction tumour positional changes. For a fixed-beam linac, the attached cone-beam imaging source and detector would also remain stationary while the patient is rotated (Feain *et al.*, 2017; Liu *et al.*, 2019). However, previous studies have shown that horizontal rotation of patients can lead to anatomical deformation (Whelan *et al.*, 2017; Buckley *et al.*, 2019). Similar anatomic deformation has also been shown in single organ and animal studies, where the anatomical deformation caused by horizontal rotation led to artefacts in the fixed-gantry CBCT reconstruction (Feain *et al.*, 2016; Barber *et al.*, 2018).

Shieh *et al.* developed an algorithm for compensating for gravity induced motion for fixed-beam CBCT scans which was tested on anaesthetised rabbits (Shieh *et al.*, 2018). However, this algorithm

compensated for only the rigid motion, and not for any complex deformable motion. It has been shown previously that for both humans (Whelan *et al.*, 2017) and rabbits (Barber *et al.*, 2018; Shieh *et al.*, 2018), the non-rigid deformation makes up a significant component of the gravity-induced motion caused by horizontal rotation. Additionally, the authors reported that for one of the rabbits, the reconstruction of the volume using their motion compensation algorithm had significant motion blur, caused by the large motion that occurred during rotation. Since only one motion compensation algorithm has been tested, alternative motion compensation algorithms may be able to improve the reconstruction quality.

Reconstruction algorithms have been developed for conventional rotating-gantry CBCT scans which use *a priori* model-based algorithms for compensating for motion (Rit *et al.*, 2009) and may use Principal Component Analysis (PCA) to adapt for current motion (Staub *et al.*, 2011; Zhang *et al.*, 2013; Harris *et al.*, 2017). Although these algorithms have proved successful using a prior 4DCT to compensate for respiratory motion, currently there is no such surrogate for the complex gravity-induced motion during horizontal patient rotation from which an *a priori* model can be created. This means it may be more difficult to accurately create an *a priori* model describing the complex gravity-induced motion caused by horizontal rotation. Because of this, the algorithms described in this paper are data-driven reconstruction algorithms, where the deformation is estimated from the data from the acquired projections.

The goal of this research is to adapt reconstruction algorithms from rotating-gantry CBCT scans to fixed-gantry CBCT scans, and to investigate how well these algorithms reconstruct fixed-gantry CBCT scans. A novel reconstruction algorithm (MCPICCS) is also introduced. This paper is the first to analyse the reconstruction quality of different reconstruction algorithms that are adapted from the rotating-gantry (stationary patient) to the fixed-gantry (rotating patient) context. This study is an important step towards being able to image rotating patients, which will meet the needs of a number of emerging treatment options as well as paving the way for future imaging systems that were previously considered infeasible.

## 2. Method

This study used fixed-gantry and rotating-gantry rotational projection images of anaesthetised rabbits, which have been previously acquired (Barber *et al.*, 2018; Shieh *et al.*, 2018) . The different fixed-gantry CBCT reconstruction algorithms are compared with the conventional rotating-gantry CBCT scans to determine which algorithms successfully compensate for horizontal rotational motion during fixed-gantry CBCT scans. For clarity, the term ‘fixed-gantry CBCT’ will be used in this paper to refer to fixed-gantry CBCT scans involving only horizontal rotation of the object being imaged. A flowchart showing the design of this study is shown in Figure 1.

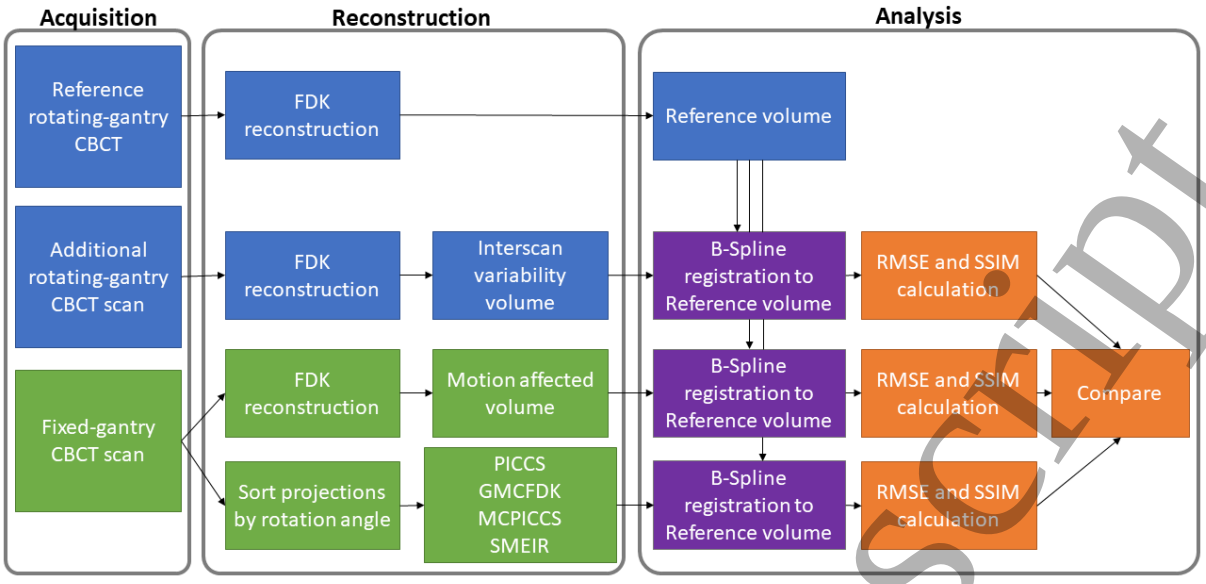


Figure 1 - Flowchart showing the study design

## 2.1 Animal preparation

Animal ethics approval was obtained prior to this study (University of Sydney Animal Ethics Committee 2015/903). Imaging was conducted using three live rabbits, weighing 351 g, 259 g and 406 g respectively and with a caudal-cranial length of 22 cm. The rabbits were anaesthetised prior to imaging and monitored throughout the experiment. For immobilisation representative of a clinical patient rotation system (Feain *et al.*, 2017), the rabbits were surrounded by bubble wrap, and then placed into a polyvinyl chloride (PVC) cradle, that allowed each rabbit to be rotated 360°, shown in Figure 2.

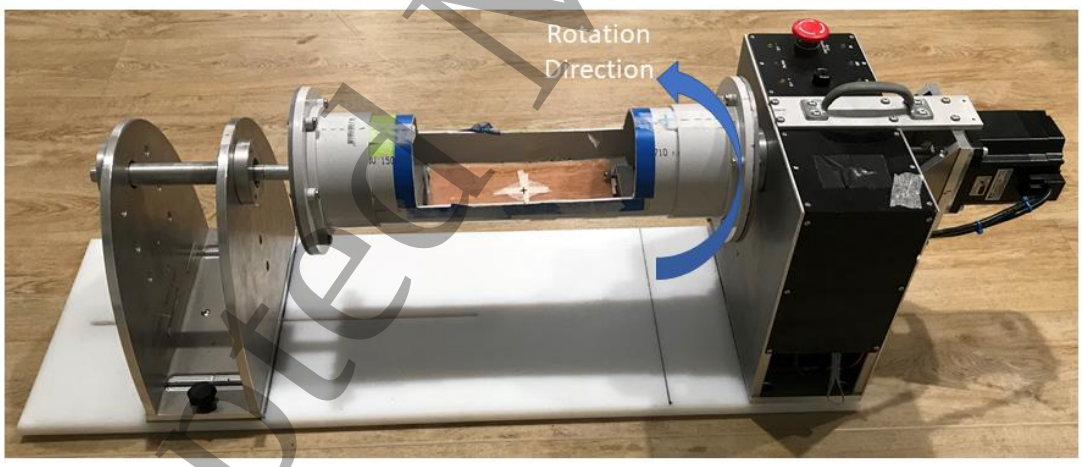


Figure 2 - The rotation cradle that the rabbits were placed in for imaging. The cradle was rotated via computer control during imaging with the angle of rotation recorded and synchronised with the kV image projection acquisition to enable CBCT image reconstruction.

## 2.2 Imaging

Imaging was conducted using the on-board kV imager of a Varian TrueBeam (Varian Medical Systems, Palo Alto, USA). This system had source to isocentre distance 1000 mm, source to detector distance 1500 mm, tube voltage 100 kVp, tube current 15 mA and exposure time 20 ms. The rabbits

were positioned such that the thoracic and abdominal regions were in the field of view. The rotation centre of the cradle holding the rabbits was aligned to the imaging isocentre.

For each rabbit, conventional (rotating-gantry) CBCT scans and fixed-gantry (rotating-rabbit) CBCT scans were acquired, with the conventional CBCT scans acting as reference volumes. For the conventional CBCT scans, the gantry rotation speed was $6^\circ\ s^{-1}$, with an angular range of 200°, and an imaging frequency 15 Hz such that for each conventional CBCT scan 490 projections were acquired. A series of conventional CBCT scans were acquired for each rabbit, with the first scan being acquired with the rabbit at 0°, and then with each subsequent scan the cradle was rotated about the horizontal axis by 45° (rotation angles 0°, 45°, 90°, 135°… to 315°). This process was repeated so that there were 16 conventional CBCT scans to act as reference volumes for different angles of rotation.

For the fixed-gantry CBCT scans, the x-ray source was fixed such that the imaging beam was vertical. The cradle holding the rabbit was rotated at $3^\circ\ s^{-1}$ to an angular range of 360° with an imaging frequency of 15 Hz, so that 1800 projections were acquired for each fixed-gantry scan. The cradle rotation angle was recorded and was used as the projection angle to create the projection geometry necessary to reconstruct the volumes.

The relatively high number of projections for the fixed-gantry and conventional CBCT scans was due to the exploratory nature of the study, given that it is not known how many projections would be needed for accurate fixed-gantry CBCT reconstructions, and what the quality of the initial reconstructions would be. Additionally, this high number of projections would ensure that any artefacts in the reconstructions would be due to the motion of the rabbit, rather than from sparse sampling or quantum noise.

## 3. Reconstruction Algorithms

In this section, the reconstruction algorithms that are used to reconstruct the fixed-gantry CBCT scans of the rotating rabbits are described, as well as the algorithm used to create the reference volume from the conventional rotating-gantry CBCT scan.

Analogous to respiratory 4DCT (Ford *et al.*, 2003; Vedam *et al.*, 2003) and 4DCBCT (Sonke *et al.*, 2005) algorithms that sort projections into bins via the respiratory phase or displacement, the acquired fixed-gantry projections were sorted into bins based on the angular rotation of the object with respect to the beam. Using the projection binning strategy described by Shieh *et al.* (Shieh *et al.*, 2018), the 8 bins were centred at 0°,45°,90°,…, 315° with width 90° so that projections belonged to multiple rotation bins i.e. the 45° bin contains projections acquired between 0° and 90°. This projection binning strategy is demonstrated in Figure 3. The projection bins created were used for all fixed-gantry reconstruction algorithms described in this paper, except for the conventional FDK. For these fixed-gantry reconstruction algorithms, the strategy of binning projections by rotation angle was the most significant step in adapting the algorithms from reconstructing rotating-gantry CBCT images to fixed-gantry CBCT images. Since projections were binned by rotation angle and not respiratory phase, respiration-related motion compensation was not applied in the application of the reconstruction algorithms.

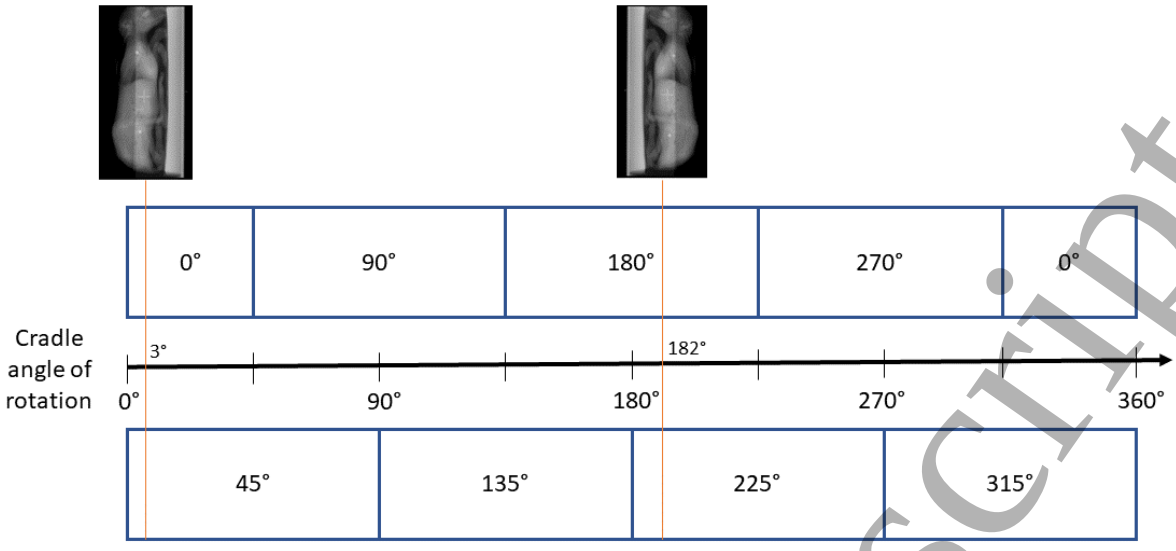


Figure 3 – A description of how the projections are sorted into different rotation bins. An example is shown where the projection acquired at 3° of rotation is sorted into both the 0° and 45° rotation bin, and where the 182° projection is sorted into both the 180° and 225° rotation bin.

For each fixed-gantry reconstruction algorithm, a volume was generated for each rotation bin (rotation angles 0°, 45°, 90°, 135°… to 315°) which was an estimation of the volume at different angles of rotation. For example, the reconstruction for the 90° rotation bin is an estimation of what the rabbit looked like when rotated 90°. These volumes will then be compared to the corresponding reference conventional CBCT scans.

In conventional respiratory motion compensation algorithms (Bergner *et al.*, 2009; Shieh *et al.*, 2019; Dillon *et al.*, 2020) and cardiac motion compensation algorithms (Mory *et al.*, 2014), most of the motion occurs in one region of interest. This means an efficient approach to computing motion in this region of interest is to assume that no motion occurs outside the region of interest. However, gravity-induced motion caused by rotation will affect the patient's whole body, and hence the whole volume. This means that any motion masking approach would not be appropriate as it would not make the computation any more efficient.

All reconstruction algorithms were implemented using the RTK toolbox (Rit *et al.*, 2014), and all registration steps were completed using the Elastix library (Klein *et al.*, 2010). For each reconstructed volume the voxel size was 0.25×0.25×0.25 $mm^3$ with dimensions 500×500×500. Reconstruction was performed on a desktop workstation with 64 GB of RAM, 32 3.1 GHz CPU cores and 2 Nvidia GPU cards with combined 3712 CUDA cores and 16 GB VRAM. The different reconstruction algorithms that were tested on the fixed-gantry CBCT scans were Feldkamp-Davis-Kress (FDK), prior image constrained compressed sensing (PICCS), gravitational motion compensated FDK (GMCFDK), motion compensated PICCS (MCPICCS) and simultaneous motion estimation and iterative reconstruction (SMEIR), which will be described below, and is summarised in Figure 4.

## 3.1 Algorithm overview

A concise mathematical summary of the algorithms used is shown in Table 1. The notation used in Table 1 is as follows: $X$ is a (vectorized) 3D volume of attenuation coefficients, $A$ is the forward projection matrix and $A^T$ the back projection matrix. Volume subscripts denote the reconstruction method and $\theta_r$ denotes a restriction to a specific rotation bin e.g. $X_{FDK,\theta_{r=1}} = X_{FDK,0}$ is the FDK reconstruction of just the data acquired at gantry angles $-45° \leq \theta \leq 45°$. $F$ is the filter matrix (e.g.

ramp, Hann) and $p$ are the (vectorized) projections. $n_\theta$ is the total number of angular bins i.e. $1 \leq r \leq n_\theta$. In PICCS, $\lambda > 0$ and $0 \leq \alpha \leq 1$ are regularization parameters. We use $TV(X)$ to denote the total variation of $X$ as

$$TV(X) = \sum_{i,j,k} \sqrt{|X(i,j,k) - X(i-1,j,k)|^2 + |X(i,j,k) - X(i,j-1,k)|^2 + \ldots \overline{|X(i,j,k) - X(i,j,k-1)|^2}} \quad (1)$$

where $X(i,j,k)$ is voxel $i,j,k$ of $X$ i.e. the sum of differences between neighbouring voxels. In GMCFDK, we define $W_{\theta_r,0}$ as the warping $X_{0,\theta_r} = W_{\theta_r,0}(X_{\theta_r,0})$ estimated using deformable image registration (DIR), and $R_{\theta_r}$ as the rigid registration of projections. In SMEIR, superscript $l$ denotes the $l$'th iteration.

Table 1 - A concise mathematical summary of the different adapted fixed-gantry CBCT reconstruction algorithms used in this paper.

| Method | Mathematical Summary | Notes |
|---|---|---|
| FDK | $X_{FDK,\theta_r} = A_{\theta_r}^T F p_{\theta_r}$ (2)<br>$X_{FDK} = A^T F p = \frac{1}{n_\theta}\sum_{r=1}^{n_\theta} X_{FDK,\theta_r} = \frac{1}{n_\theta}\sum_{r=1}^{n_\theta} A_{\theta_r}^T F p_{\theta_r}$ (3) | Standard FDK with filtered backprojection. Volumes for each rotation bin are equal and independent of projection rotation angle. |
| PICCS | $X_{PICCS,\theta_r} = \min_X \left\{ \left\| A_{\theta_r} X - p_{\theta_r} \right\|_2^2 + \lambda\left((1-\alpha)TV(X) + \alpha TV\left(X - X_{prior}\right)\right)\right\}$ (4) | Prior volume is FDK reconstruction. |
| GMCFDK | $X_{GMCFDK,0}^{\text{initial}} = \frac{1}{n_\theta}\sum_{r=1}^{n_\theta} W_{\theta_j,0}\left(X_{FDK,\theta_r}\right) = \frac{1}{n_\theta}\sum_{r=1}^{n_\theta} W_{\theta_j,0}\left(A_{\theta_r}^T F p_{\theta_r}\right)$ (5)<br>$R_{\theta_r} = \min_R \{A_{\theta_r} X_{GMCFDK,0}^{init} - R(p_{\theta_r})\}$ (6)<br>$X_{GMCFDK,0} = \frac{1}{n_\theta}\sum_{r=1}^{n_\theta} W_{\theta_r,0}\left(A_{\theta_r}^T F R_{\theta_r}(p_{\theta_r})\right) X_{GMCFDK,\theta_r} = W_{0,\theta_r}\left(X_{GMCFDK,0}\right)$ (7) | Projections are warped for initial GMCFDK. Volumes forward projected and registered to original projections. |
| MCPICCS | $X_{0,\theta_r} = W_{\theta,0}\left(X_{PICCS,\theta_r}\right)$ (8)<br>$X_{MCPICCS,0}^{\text{initial}} = \frac{1}{n_\theta}\sum_{r=1}^{n_\theta} W_{\theta_j,0}\left(X_{PICCS,\theta_r}\right)$ (9)<br>$X_{MCPICCS,\theta_r}^{\text{initial}} = W_{0,\theta_r}\left(X_{MCPICCS,0}^{\text{initial}}\right)$ (10)<br>$X_{MCPICCS,\theta_r} = \min_X \{\|AX - p_\theta\|_2^2 + TV(X)\}$ (11) | Motion Compensation from PICCS volumes. Motion Compensated volumes used as initial estimates for total variation reconstruction. |

| | | |
|---|---|---|
| SMEIR | $$X_{SMEIR,\theta_r}^{l+1} = \min_X \left\{ \left\| \sum_{k=1}^{n_\theta} A_{\theta_k} W_{\theta_j,\theta_k}^{l}(X) - p_{\theta_k} \right\|_2^2 + \mathrm{TV}(X) \right\} \quad (12)$$ $$X_{SMEIR,\theta_r}^{l+1} = W_{\theta_k,\theta_r}^{l+1}\left(X_{SMEIR,\theta_k}^{l+1}\right) \quad (13)$$ | At each iteration, perform a motion compensated total variation regularised reconstruction, then use that reconstruction to estimate a new motion model. |

## 3.2 FDK

Each conventional rotating-gantry CBCT scan was reconstructed using the FDK algorithm (Feldkamp, Davis and Kress, 1984) and a Hann smoothing parameter of 0.7 to create the reference volumes. These parameters were also used to create fixed-gantry FDK reconstruction volumes. The fixed-gantry FDK reconstructions used all acquired projections instead of the binned projections, because the binned angular range was too small to produce meaningful fixed-gantry binned FDK reconstruction volumes. As such we expect the fixed-gantry FDK reconstructions to contain significant motion blur.

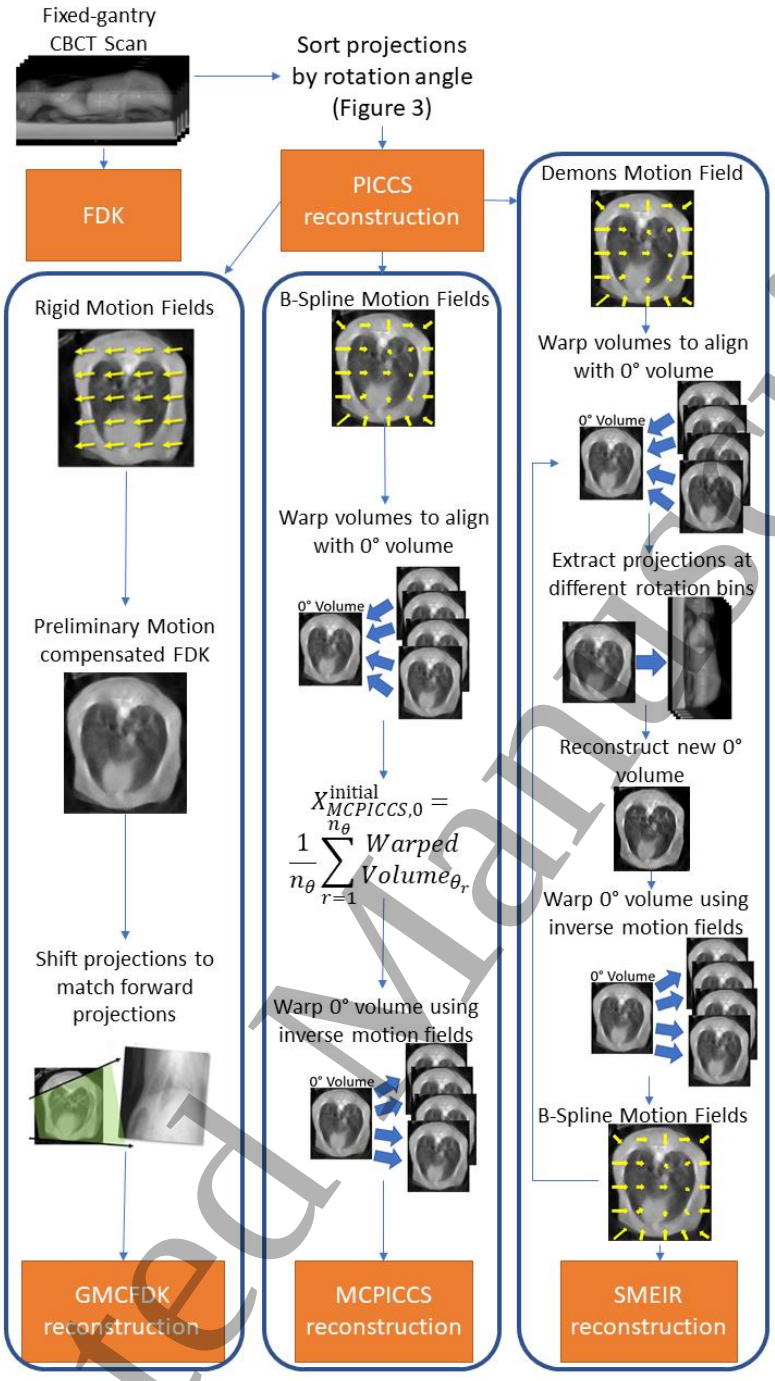


Figure 4 - A summary of the fixed-gantry reconstruction algorithms

### 3.3 PICCS

PICCS is an image reconstruction algorithm that can use a prior image and a limited range of projections to reconstruct a volume (Chen, Tang and Leng, 2008). This reconstruction algorithm attempts to compute a volume that fits the binned projections, while being similar to the prior volume, with a sparse image gradient (i.e. homogeneous regions with a few well-defined edges). Given that the binned projections have an angular range of 90°, PICCS is an appropriate algorithm for estimating the volumes for the different rotation bins, and has been previously shown to be able to reconstruct volumes from fixed-gantry CBCT scans with a limited angular projection range (Feain *et al.*, 2016; Shieh *et al.*, 2018). For this implementation of PICCS, the prior volume was the fixed-gantry

FDK reconstructed volume, generated from all of the projections acquired with the object rotating. The regularisation parameters (see equation 4 in Table 1) $\lambda$ and $\alpha$ were set to 1 and 0.5 respectively.

### 3.4 Gravitational Motion Compensated FDK

Conventional 4DFDK (Sonke *et al.*, 2005) computes respiratory phase correlated volumes by filtering and back projecting only those projections acquired at the desired respiratory phase. The Motion Compensated FDK (MCFDK) algorithm introduced by Rit *et al.* (Rit *et al.*, 2009) produces phase correlated volumes by filtering and back projecting all acquired projections, but along curved paths to account for out-of-phase respiratory motion. The application of MCFDK to gravitationally induced motion was introduced by Shieh *et al.* (Shieh *et al.*, 2018), and has demonstrated the ability to reconstruct volumes from fixed-gantry CBCT scans. In the algorithm proposed by Shieh *et al.*, first the projections were binned by rotation angle and PICCS reconstructions were performed as detailed above. The PICCS-reconstruction volumes were then deformably registered to each other to produce deformation vector fields (DVFs) estimating the motion between rotation bins. These motion estimates were then used with the rotation binned projections in the MCFDK algorithm to produce an initial GMCFDK volume. This volume was then forward projected to create simulated projections. The measured projections were rigidly registered to the simulated projections to produce translated measured projections, accounting for the bulk motion of the rabbit in the cradle. The PICCS motion estimates and rotation binned translated measured projections were used in the MCFDK algorithm to produce final GMCFDK volumes.

### 3.5 Motion Compensated PICCS

The MCPICCS algorithm is a novel adaptation of previously described motion compensation reconstruction algorithms such as the MCFDK algorithm by Riblett *et al.* (Riblett *et al.*, 2018) and the Motion Compensated McKinnon-Bates (MCMKB) algorithm by Dillon *et al.* (Dillon *et al.*, 2020). These motion compensation reconstruction algorithms have shown an ability to reconstruct motion compensated 4D-CBCT scans, which is why this algorithm has been chosen for this study.

In the MCPICCS algorithm, similarly to the GMCFDK algorithm described in section 3.4, all PICCS volumes are deformably registered to the PICCS volume from the 0° rotation bin using a B-spline registration method to estimate DVFs describing the motion between rotation bins. Each volume is then warped using the estimated DVFs to be aligned with the 0° PICCS volume. A new 0° volume is then calculated by averaging all warped volumes. The new 0° volume is then warped using the inverse DVFs to generate volumes for the other rotation bins. We refer to these volumes as MCPICCS initial volumes.

The MCPICCS initial volumes had minimal motion artefacts but were blurry. The blurry images were likely caused by the DVFs being an inexact estimate of the motion between rotation bins phases causing the volumes that are deformed to match the base volume not correctly aligning. To improve the quality of the MCPICCS volumes, the MCPICCS initial volumes were used as initial estimates for a total variation (TV) regularised reconstruction (equation 11), computing a volume that fitted the binned projections with a sparse image gradient similar to PICCS, creating the final MCPICCS volumes.

### 3.6 SMEIR

The SMEIR algorithm (Wang and Gu, 2013) iteratively estimates both the anatomy and motion. At each iteration $l$, phase correlated volumes are computed that, given the current motion model, matches the data and have sparse image gradients. In Wang and Gu, 2013 the $l = 0$ iteration takes null volumes and motion models, however we initialised with PICCS volumes to account for the limited view angles complicating initial convergence. The computed volumes make up the iteration $l + 1$ SMEIR volumes. The volumes are then deformably registered to each other to create the

iteration $l+1$ SMEIR motion models. The registration of the initial volumes used a demons registration algorithm, and then for the volumes in the iteration a B-Spline deformation algorithm was used, as described in the respiratory motion SMEIR paper (Wang and Gu, 2013). The original SMEIR paper bins the volumes by respiratory phase, while in our case we bin by rotation angle. Additionally, the original SMEIR paper uses the SART reconstruction method, but as shown in Table 1 shows, for the fixed-gantry implementation a TV reconstruction method was used. Hence the implementation of SMEIR used in this paper was adapted from the original SMEIR implementation to account for the gravitational motion caused by horizontal rotation.

### 3.7 Image quality metrics

For each rotation bin (rotation angles 0°, 45°, 90°, 135°… to 315°), the volumes from the different fixed-gantry reconstruction algorithms were compared with the corresponding reference volume from the conventional CBCT scan. To compare the quality of the reconstructed volumes, the image metrics root-mean-square error (RMSE), the structural similarity index measure (SSIM) and the reconstruction time were used. Similarly to Sheih *et al.* (Shieh *et al.*, 2018), the RMSE and SSIM analysis was conducted in a pre-defined region of interest, specifically the lungs. The RMSE and SSIM values were calculated as:

$$RMSE = \frac{1}{\sqrt{n}} \left\| X_{Ref} - X_{Recon} \right\|_2 \tag{14}$$

$$SSIM = \frac{(2\mu_{Ref}\mu_{Recon} + c_1)(2\sigma_{Ref,Recon} + c_2)}{(\mu_{Ref}^2 + \mu_{Recon}^2 + c_2)(\sigma_{Ref}^2 + \sigma_{Recon}^2 + c_2)} \tag{15}$$

where $n$ is the number of voxels, $X$ are the voxel values within the lung boundaries as described in Shieh *et al.* (Shieh *et al.*, 2018), $\mu$ and $\sigma$ are the voxel mean and variance values respectively, the subscript $Ref$ refers to the reference volume and $Recon$ refers to the reconstruction algorithm being evaluated, and $c_1 = (0.01L)^2$ and $c_2 = (0.03L)^2$ where $L$ is the dynamic range of the volumes. The time taken for each reconstruction to be completed was also recorded for one rabbit at one rotation bin and compared for the different reconstruction methods.

Although the reference conventional CBCT volumes provide an estimation of the expected deformation that occurs during rotation of the rabbit, because of intra-bin motion and possible inter-rotation irreproducibility there will be some difference between the reference conventional CBCT volume and a perfectly reconstructed fixed-gantry CBCT volume. Hence for each rabbit, a minimum of two conventional CBCT scans were acquired, as described in section 2.2, with the first scan being a reference volume, and the second volume an additional conventional CBCT volume. For each rotation bin, the SSIM and RMSE were also calculated between the reference and the additional conventional CBCT volumes to provide an estimation as to the normal level of variability between conventional rotating-gantry CBCT scans. This variability will act as a benchmark to indicate the difference in quality between a conventional CBCT scan, and a fixed-gantry CBCT scan reconstructed using motion compensation algorithms.

Additionally, because of the inter-rotation motion, for each SSIM and RMSE calculation the non-reference volume was deformably registered to the reference volume, using a B-Spline registration. The registration was performed to ensure that any differences that would contribute to the RMSE and SSIM values were because of the effectiveness of the reconstruction algorithm, and not because of any differences in anatomy between rotations.

# 4. Results

## 4.1 Visual Analysis

The results of the different fixed-gantry CBCT reconstructions for rabbit 1, 2 and 3 are shown in Figure 5. These figures show that for all rabbits, when compared to the reference volume (conventional rotating-gantry CBCT), the fixed-gantry FDK did not accurately reconstruct the motion affected projections, causing blurred, inaccurate volume reconstructions. This result has been observed in previous fixed-gantry CBCT studies (Feain *et al.*, 2016; Shieh *et al.*, 2018).

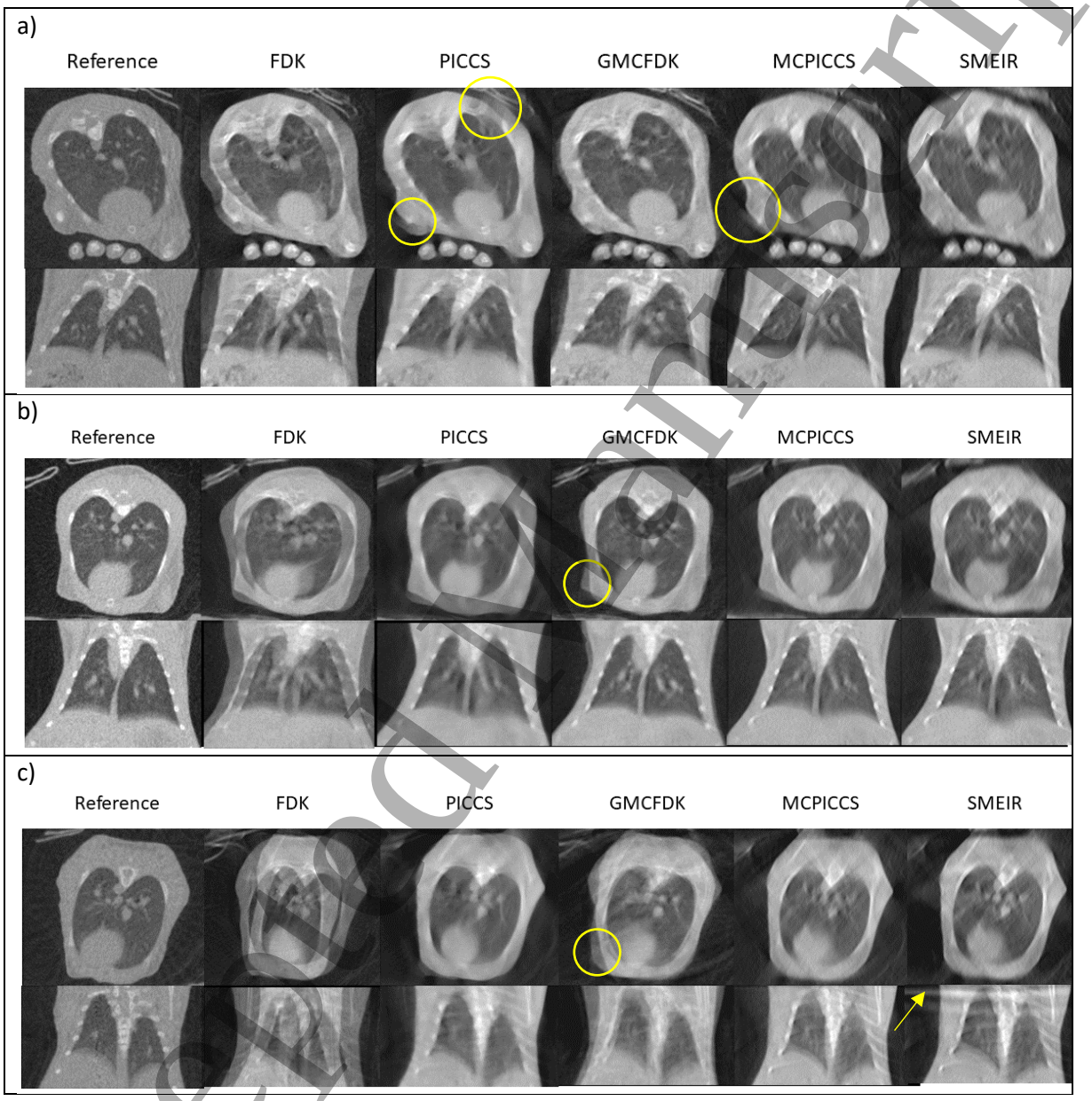


Figure 5 - Images of rabbit 1 (a), rabbit 2 (b) and rabbit 3 (c) lungs from axial (top) and coronal (bottom) slices from different reconstruction methods for the 0° rotation bin. Windowing level [0,0.03] $mm^{-1}$. Image reconstruction artefacts discussed in the text have been highlighted in yellow.

The images from the PICCS reconstruction algorithm in Figure 5 show less motion blur when compared to the conventional FDK algorithm. The images from the PICCS algorithm also more closely resemble the images from the reference CBCT than the conventional FDK images. These figures demonstrate why the PICCS reconstruction algorithm is used to generate an initial estimate

for the SMEIR algorithm, as it allows for a quick approximate volume to be generated, so that initial DVF estimates can be calculated. However, Figure 5(a) (rabbit 1) shows that motion artefacts still occur at the outer edges of the rabbit (highlighted by the yellow circles).

The images from the GMCFDK reconstruction more closely resemble the reference images from the conventional CBCT than the images from the PICCS and FDK fixed-gantry reconstruction algorithms. Additionally, for rabbits 1 and 2, when compared with the MCPICCS and SMEIR methods, the GMCFDK reconstruction allows for better definition of bronchi inside the lungs in the axial plane (Figure 5(a) and (b)). For rabbit 3 (Figure 5(c)), the images from the MCPICCS and SMEIR reconstruction algorithms show similar levels of detail of these smaller features to the image from the GMCFDK reconstruction algorithm. Conversely, in rabbits 2 and 3, (Figure 5(b) and (c)) the outer border of the volumes reconstructed using the GMCDFK algorithm is poorly defined, as highlighted in Figure 5(c). This effect is more prominent in rabbit 3, where the magnitude of the rigid motion was larger than for the other rabbits (Barber *et al.*, 2018; Shieh *et al.*, 2018).

An example of how the MCPICCS is able to improve the quality of the fixed-gantry CBCT reconstruction is shown in Figure 6. The motion compensation component of the MCPICCS algorithm is able to reduce motion artefacts between the PICCS and the initial MCPICCS volume. The TV step increases the quality of the MCPICCS image to generate the final MCPICCS volume. This example demonstrates the need for each step of the reconstruction process in the MCPICCS algorithm.

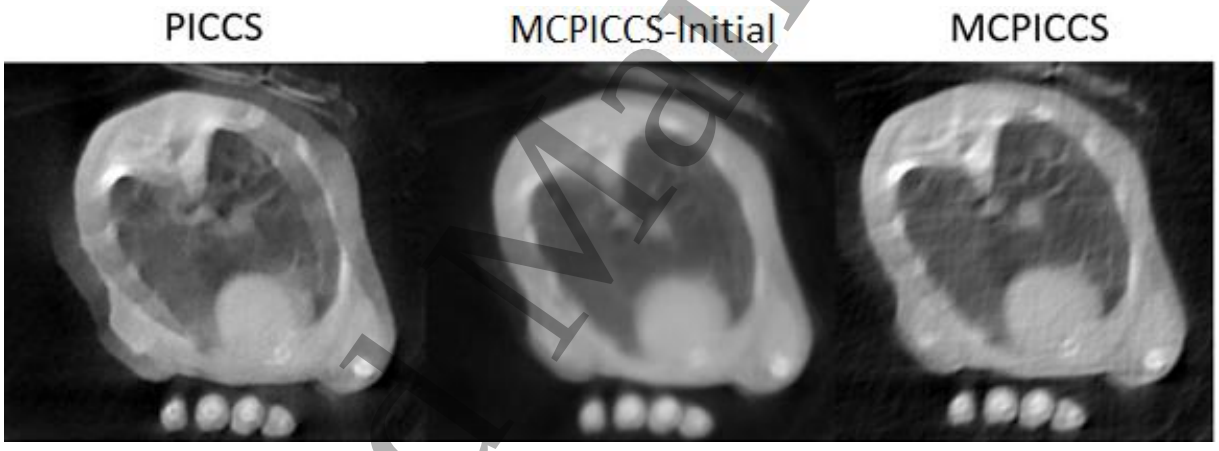


Figure 6 - An example of the MCPICCS algorithm. The initial PICCS volumes (left) have the motion compensation applied (middle) which produces a slightly blurry image. This quality of the MCPICCS image is improved using Total Variation reconstruction (right) with the MCPICCS as the initial volume. Windowing level [0,0.03] $mm^{-1}$

The results in Figure 5 show that the MCPICCS algorithm generated higher quality images that more closely match the reference volume from the conventional CBCT than the standard PICCS algorithm. The images from the MCPICCS reconstruction algorithm also have a relatively well-defined border, although there are still some artefacts at the border as highlighted in Figure 5 (a). These results demonstrate the effectiveness of the motion compensation in the MCPICCS algorithm for increasing the reconstruction quality.

Figure 5 additionally shows that the SMEIR algorithm, when compared with the reference volume from the conventional CBCT, was also able to reconstruct the fixed-gantry CBCT scans accurately. For rabbits 1 and 2 (Figure 5 (a) and (b)), the SMEIR algorithm was able to reconstruct a volume with both a well-defined outer boundary and features inside the lungs. When reconstructing the scans from rabbit 3 using SMEIR, artefacts occurred in the lungs, as shown by the arrow in Figure 5 (c).

These artefacts are boundary artefacts arising due to the repeated use of the total variation reconstruction algorithm. This artefact is only visible for rabbit 3 because for the animal was positioned such that the lung was on the border of the CBCT image space as shown by the arrows in Figure 5 (c) and Figure 7.

Figure 7 - Full view of the SMEIR reconstruction of rabbit 3 showing how the lung is at the image border. The border artefacts are indicated by yellow arrows. Windowing level [0,0.03] $mm^{-1}$.

## 4.2 Quantitative Analysis

The results for Figure 5 are only for when the volume was at 0° rotation, however the volumes were reconstructed at multiple angles of rotation, as described in section 2.2. Figure 8 compares the RMSE and SSIM values for the different reconstruction algorithms for all rabbits at all rotation bins with the conventional rotating-gantry CBCT volumes used as the reference volume. An additional conventional rotating-gantry CBCT volume was also used to illustrate the variability in conventional CBCT scans, and hence the ideal variability for the fixed-gantry CBCT reconstructions.

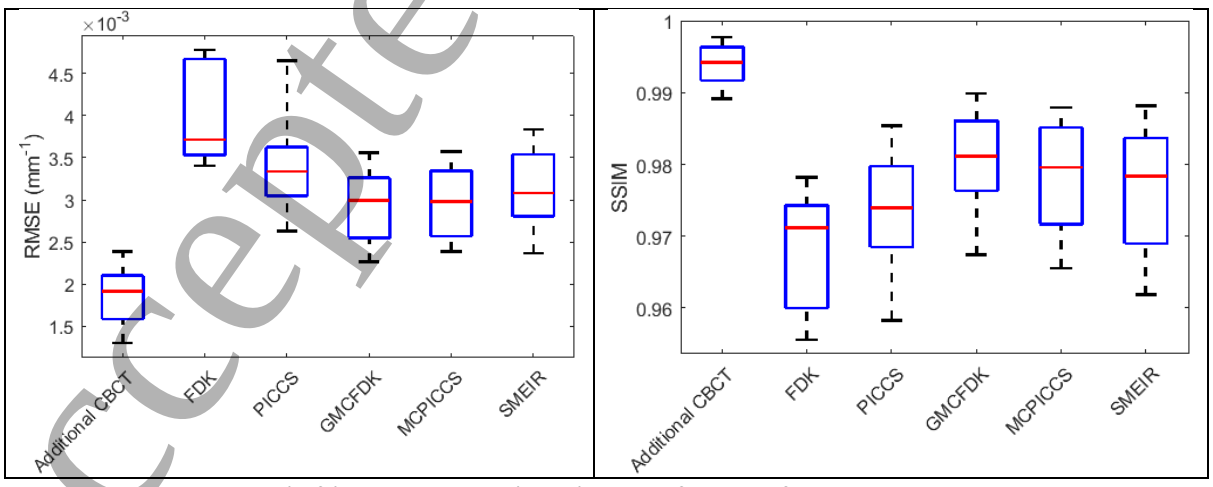


Figure 8 - The RMSE (left) and the SSIM (right) values for each fixed-gantry CBCT reconstruction method when the reconstructed volume was compared with a reference rotating-gantry CBCT volume. An additional rotating-gantry CBCT was also included to show normal variation between

rotating-gantry CBCT volumes. An ideal volume would have a lower RMSE value and a higher SSIM value.

Figure 8 shows that all motion compensation reconstruction methods (GMCFDK, MCPICCS, SMEIR) were able to increase the quality of the volume reconstruction when compared with the fixed-gantry FDK. There was a reduction of approximately 6.4-7.2×$10^{-3}$ $mm^{-1}$ (17-19% reduction) in the median RMSE values for the GMCFDK, MCPICCS and SMEIR methods and an increase in the median SSIM values of approximately 1%, when compared with the fixed-gantry FDK. The high SSIM values also indicate the reconstructions were of a high similarity to the volumes from the conventional CBCT scans. These quantitative metrics mirror the observations recorded previously from Figure 5.

Figure 8 shows that the MCPICCS algorithm produces a volume with a lower RMSE value and a higher SSIM value than the conventional PICCS algorithm. This suggests that, as observed in Figure 5 the motion compensation and TV reconstruction steps used in the MCPICCS algorithm increase the quality of the reconstruction. Similarly, the lower RMSE values and higher SSIM values between the GMCFDK and conventional FDK reconstruction algorithms demonstrate the effectiveness of the rotational motion compensation steps in the GMCFDK reconstruction algorithm.

Figure 8 shows that although the different fixed-gantry CBCT reconstruction algorithms were able to increase the quality of the volumes (lower RMSE and higher SSIM), the median RMSE values were approximately 1.1-1.2×$10^{-3}$ $mm^{-1}$ higher (a relative increase of approximately 56-61%) and the SSIM values were 1.5% lower than the corresponding RMSE and SSIM values for the additional rotating-gantry CBCT scan. This suggests that in this experiment for the fixed-gantry CBCT reconstruction algorithms described in this paper, there is a quantitative difference between reconstructions from fixed-gantry CBCT scans and the FDK reconstructions of the rotating-gantry CBCT scans.

### 4.3 Reconstruction Time

The time taken for each of the fixed-gantry reconstruction algorithm is shown in Table 2. These times were for one fixed-gantry and one rotating-gantry CBCT scan for Rabbit 1. This table shows that the fastest reconstruction times were for the FDK reconstruction algorithm of the conventional and fixed-gantry CBCT scans. The PICCS algorithm took longer than the FDK algorithm, however, the algorithms with motion compensation steps (GMCFDK, MCPICCS and SMEIR) took longer than both the PICCS and FDK algorithms, suggesting that the motion compensation algorithms add time to the reconstruction process. The SMEIR algorithm took the longest amount of time, which was probably a result of iterative motion compensation process involved in SMEIR, instead of a single motion compensation step used in the GMCFDK and MCPICCS algorithms.

Table 2 – A comparison of the time taken for each reconstruction algorithm to reconstruct one CBCT scan.

| Reconstruction algorithm | Reconstruction time |
|---|---|
| Conventional CBCT FDK | 26.64 seconds |
| Fixed-gantry CBCT FDK | 1.2 minutes |
| PICCS | 41.6 mins |
| GMCFDK | 5.8 hours |
| MCPICCS | 2.8 hours |
| SMEIR | 96 hours |

## 5. Discussion

In this research project, different motion compensation algorithms were adapted to reconstruct fixed-gantry CBCT scans and the effectiveness of these algorithms were investigated using scans acquired from anaesthetised rabbits. The reconstruction algorithms were compared using the SSIM, RMSE and reconstruction time metrics, which were compared with FDK reconstructions of conventional rotating-gantry CBCT scans as the reference volumes. The driver of this study was that the different motion compensation algorithms were able to increase the accuracy of the reconstruction of the fixed-gantry CBCT data when compared with a traditional FDK reconstruction. For the acquired data, this hypothesis was confirmed visually in Figure 5, as well as quantitatively in Figure 8.

The results in this paper have demonstrated that for all fixed-gantry reconstruction algorithms the SSIM and RMSE metrics of the reconstructed volumes were worse than the conventional rotating-gantry CBCT reconstructions. Since humans are larger and weigh more than rabbits, it is expected for humans that the deformation caused by horizontal rotation will be larger than for rabbits. Buckley *et al*. (Buckley *et al.*, 2019) showed that the magnitude of deformation of humans during horizontal rotation, was larger than the measured deformation magnitude from the rabbits as reported by Barber *et al.* (Barber *et al.*, 2018). To compensate for the deformation expected in humans, the patient rotation system described by Liu *et al.* has been designed to be more robust in limiting motion during rotation, through the use of inflated airbags and chest straps (Liu *et al.*, 2019). However, significant deformation of humans is still expected to occur during rotation. Additionally, the number of acquired projections for humans will be reduced when compared to the number of projections used in this paper, which may also alter the results. Future studies will investigate whether the reconstruction methods described in this paper will be able to produce clinically usable images from fixed-gantry CBCT scans of humans.

The MCPICCS algorithm described in this paper has a final TV reconstruction step which is used to increase the quality of the reconstruction, as shown in Figure 6. In previous implementations of this motion compensation algorithm (Riblett *et al.*, 2018; Dillon *et al.*, 2020), this step has not been required, as the motion compensation steps have been sufficient to produce a high quality volume. This suggests that the gravity-induced motion caused by rotating the rabbits produces motion that is more complex than in previously implemented applications of the described motion compensation algorithm. It is possible that the TV reconstruction step could be removed if other methods for estimating motion can better estimate the motion between phases, such as the iterative algorithm described in the SMEIR algorithm (Wang and Gu, 2013) or the Robust PCA algorithm (Zhi, Kachelrieß and Mou, 2020).

Similarly, the GMCFDK algorithm described by Shieh *et al.* assumes the motion of the rabbits can be approximated by rigid motion. It was observed that a disadvantage of the GMCFDK algorithm is that the borders of the reconstructed volumes are not well defined. It is thought that this is because only the rigid motion is accounted for in the motion compensation steps. Hence, using more complex deformation models could allow for more accurate motion compensation algorithms, and hence more accurate volume reconstructions.

Table 2 shows that the implementation of the adapted SMEIR algorithm in this paper takes several days. The large implementation time is not unexpected as in previous implementations of SMEIR, the authors commented on the lengthy implementation times (Wang and Gu, 2013; Huang, Zhang and Wang, 2018). Table 2 also shows that on the same computer the GMCFDK and MCPICCS reconstruction algorithms were faster, taking only several hours, including the PICCS reconstruction

step. For all of the motion compensated reconstruction algorithms described in this paper, the computation time would make it difficult to do on-the-fly reconstruction, similarly to the FDK reconstructions and the algorithms described by Rit et al. (Rit *et al.*, 2009).

The authors of the SMEIR algorithm were able to increase the accuracy of the reconstructions by adding a biomechanical modelling element into the reconstruction algorithm (Huang, Zhang and Wang, 2018). The biomechanical model used a physics-based model to estimate the motion of the lung to improve the accuracy of the DVFs. The advantage of this algorithm is that it can add extra information to the reconstruction to increase the reconstruction accuracy, which is particularly useful when there are limited projection numbers. Given that the deformation due to rotation will vary depending on the tissue material properties and can produce complex DVFs, adding a biomechanical modelling element to the reconstruction algorithms described in this paper could provide more accurate DVFs between motion phases. This could be used to increase the accuracy of the fixed-gantry CBCT reconstruction algorithms.

Since the rabbits that were imaged were anaesthetised, there would have been some respiratory motion in the acquired projections that was not compensated for. This motion would have caused some motion artefacts in the lungs, particularly around the diaphragm (Low *et al.*, 2003; Sonke *et al.*, 2005). Barber *et al.* showed that using a conventional CBCT scan of the rabbits, the magnitude of the respiratory motion during a conventional 4D CBCT scan did not vary with changing angles of rotation (Barber *et al.*, 2018). Future implementations of motion compensation algorithms described here could expand to gravitational and respiratory motion compensation, similar to the simultaneous respiratory and cardiac compensation described by Sauppe *et al.* (Sauppe *et al.*, 2016).

Shieh *et al.* noted that some of the deformation due to gravity could be hidden from the captured kV images as the imaging direction was parallel to gravity (Shieh *et al.*, 2018). However, in the prototype patient rotation system developed by Liu *et al.* (Liu *et al.*, 2019) the treatment beam source would be above the patient, with the direction of the treatment beam parallel to gravity. The kV imaging beam would instead be perpendicular to the treatment beam. It is unknown where the optimal position of the kV imaging beam would be, such that motion artefacts in the reconstruction are minimised, and this will need to be investigated in future studies.

## 6. Conclusion

Motion compensation algorithms developed for reconstruction of conventional rotating-gantry CBCT scans were adapted to reconstruct volumes for fixed-gantry CBCT scans of anaesthetised rabbits. Adapted versions of PICCS, GMCFDK, and SMEIR as well as a custom MCPICCS algorithm, were compared against a conventional FDK reconstruction on the fixed-gantry and the conventional rotating-gantry CBCT scans. The results showed that the GMCFDK, MCPICCS and SMEIR algorithms were able to increase the quality of the fixed-gantry CBCT reconstructions, as well as reducing the RMSE and increasing the SSIM. However, the fixed-gantry reconstruction methods had a 56-61% higher RMSE value and a 1.5% lower SSIM than a conventional FDK reconstruction of a rotating-gantry CBCT scan. The motion compensation algorithms described in this paper were able to visibly reduce motion artefacts showing that high quality reconstructions from fixed-gantry CBCT scans are possible. This work will help the development of compact, low-cost linacs to address the rising global demand for radiotherapy.

## Acknowledgements

The authors wish to acknowledge the work of William Counter, Ilana Feain, Jonathan Sykes and Paul White in assisting in the data collection, and Paul Liu in assisting with the figures. Helen Ball

reviewed and improved the clarity of the manuscript. Funding for this work included an Australian Government NHMRC Development Grant and an NHMRC Senior Principal Research Fellowship. RO was supported by a Cancer Institute NSW Career Development Fellowship.

## 7. References

Atun, R. *et al.* (2015) 'Expanding global access to radiotherapy', *The Lancet Oncology*. Lancet Publishing Group, pp. 1153–1186. doi: 10.1016/S1470-2045(15)00222-3.

Barber, J. *et al.* (2018) 'A CBCT study of the gravity-induced movement in rotating rabbits', *Physics in Medicine & Biology*, 63(10), p. 105012. doi: 10.1088/1361-6560/aabf12.

Bergner, F. *et al.* (2009) 'Autoadaptive phase-correlated (AAPC) reconstruction for 4D CBCT', *Medical Physics*. John Wiley and Sons Ltd, 36(12), pp. 5695–5706. doi: 10.1118/1.3260919.

Buckley, J. G. *et al.* (2019) 'Anatomical deformation due to horizontal rotation: towards gantry-free radiation therapy', *Physics in Medicine & Biology*. IOP Publishing, 64(17), p. 175014. doi: 10.1088/1361-6560/ab324c.

Buckley, J. G. *et al.* (2021) 'Measurements of human tolerance to horizontal rotation within an MRI scanner: Towards gantry-free radiation therapy', *Journal of Medical Imaging and Radiation Oncology*. Blackwell Publishing, 65(1), pp. 112–119. doi: 10.1111/1754-9485.13130.

Buckley, J. G., Dong, B. and Liney, G. P. (2020) 'Imaging performance of a high-field in-line magnetic resonance imaging linear accelerator with a patient rotation system for fixed-gantry radiotherapy', *Physics and Imaging in Radiation Oncology*. Elsevier, 16, pp. 130–133. doi: 10.1016/j.phro.2020.11.001.

Chen, G. H., Tang, J. and Leng, S. (2008) 'Prior image constrained compressed sensing (PICCS): A method to accurately reconstruct dynamic CT images from highly undersampled projection data sets', *Medical Physics*. John Wiley and Sons Ltd, 35(2), pp. 660–663. doi: 10.1118/1.2836423.

Debrot, E. *et al.* (2020) 'Will Patients Accept Horizontal Rotation During Radiotherapy Treatment? Patient Reported Outcomes of Rotation On a Prototype Fixed Beam Radiotherapy System. (Abstract)', in *2020 Joint American Association of Physicists in Medicine (AAPM) and Canadian Organization of Medical Physicists (COMP)*. Vancouver (virtual).

Devicienti, S. *et al.* (2010) 'Patient positioning in the proton radiotherapy era', *Journal of Experimental and Clinical Cancer Research*. BioMed Central Ltd., p. 47. doi: 10.1186/1756-9966-29-47.

Dillon, O. *et al.* (2020) 'Evaluating reconstruction algorithms for respiratory motion guided acquisition', *Physics in Medicine & Biology*. IOP Publishing, 65(17), p. 175009. doi: 10.1088/1361-6560/ab98d3.

Eslick, E. M. and Keall, P. J. (2015) 'The Nano-X Linear Accelerator', *Technology in Cancer Research & Treatment*, 14(5), pp. 565–572. doi: 10.7785/tcrt.2012.500436.

Feain, I. *et al.* (2016) 'Functional imaging equivalence and proof of concept for image-guided adaptive radiotherapy with fixed gantry and rotating couch', *Advances in radiation oncology*, 1(4), pp. 365–372. doi: 10.1016/j.adro.2016.10.004.

Feain, I. *et al.* (2017) 'Technical Note: The design and function of a horizontal patient rotation system for the purposes of fixed-beam cancer radiotherapy', *Medical Physics*. John Wiley & Sons, Ltd, 44(6), pp. 2490–2502. doi: 10.1002/mp.12219.

Feldkamp, L. A., Davis, L. C. and Kress, J. W. (1984) 'Practical cone-beam algorithm', *Journal of the*

*Optical Society of America A*. Optical Society of America, 1(6), p. 612. doi: 10.1364/JOSAA.1.000612.

Ford, E. C. *et al.* (2003) 'Respiration-correlated spiral CT: A method of measuring respiratory-induced anatomic motion for radiation treatment planning', *Medical Physics*. John Wiley and Sons Ltd, 30(1), pp. 88–97. doi: 10.1118/1.1531177.

Harris, W. *et al.* (2017) 'Estimating 4D-CBCT from prior information and extremely limited angle projections using structural PCA and weighted free-form deformation for lung radiotherapy', *Medical physics*, 44(3), pp. 1089–1104. doi: 10.1002/mp.12102.

Huang, X., Zhang, Y. and Wang, J. (2018) 'A biomechanical modeling-guided simultaneous motion estimation and image reconstruction technique (SMEIR-Bio) for 4D-CBCT reconstruction.', *Physics in medicine and biology*, 63(4), p. 045002. doi: 10.1088/1361-6560/aaa730.

Klein, S. *et al.* (2010) 'Elastix: a toolbox for intensity-based medical image registration', *IEEE Transactions on Medical Imaging*, 29(1), pp. 196–205. doi: 10.1109/TMI.2009.2035616.

Liu, P. Z. Y. *et al.* (2019) 'Development and commissioning of a full-size prototype fixed-beam radiotherapy system with horizontal patient rotation', *Medical Physics*. John Wiley and Sons Ltd., 46(3), pp. 1331–1340. doi: 10.1002/mp.13356.

Low, D. A. *et al.* (2003) 'A method for the reconstruction of four-dimensional synchronized CT scans acquired during free breathing', *Medical Physics*. John Wiley and Sons Ltd, 30(6), pp. 1254–1263. doi: 10.1118/1.1576230.

Mory, C. *et al.* (2014) 'Cardiac C-arm computed tomography using a 3D + time ROI reconstruction method with spatial and temporal regularization', *Medical Physics*. John Wiley & Sons, Ltd, 41(2), p. 021903. doi: 10.1118/1.4860215.

Riblett, M. J. *et al.* (2018) 'Data-driven respiratory motion compensation for four-dimensional cone-beam computed tomography (4D-CBCT) using groupwise deformable registration', *Medical Physics*. John Wiley and Sons Ltd., 45(10), pp. 4471–4482. doi: 10.1002/mp.13133.

Rit, S. *et al.* (2009) 'On-the-fly motion-compensated cone-beam CT using an a priori model of the respiratory motion', *Medical Physics*, 36(6Part1), pp. 2283–2296. doi: 10.1118/1.3115691.

Rit, S. *et al.* (2014) 'The Reconstruction Toolkit (RTK), an open-source cone-beam CT reconstruction toolkit based on the Insight Toolkit (ITK)', in *Journal of Physics: Conference Series*. Institute of Physics Publishing. doi: 10.1088/1742-6596/489/1/012079.

Sauppe, S. *et al.* (2016) 'Five-dimensional motion compensation for respiratory and cardiac motion with cone-beam CT of the thorax region', in Kontos, D., Flohr, T. G., and Lo, J. Y. (eds) *Medical Imaging 2016: Physics of Medical Imaging*. SPIE, p. 97830H. doi: 10.1117/12.2216266.

Shieh, C.-C. *et al.* (2018) 'Cone-beam CT reconstruction with gravity-induced motion', *Physics in Medicine & Biology*, 63(20), p. 205007. doi: 10.1088/1361-6560/aae1bb.

Shieh, C. C. *et al.* (2019) 'SPARE: Sparse-view reconstruction challenge for 4D cone-beam CT from a 1-min scan', *Medical Physics*. John Wiley and Sons Ltd, 46(9), pp. 3799–3811. doi: 10.1002/mp.13687.

Sonke, J. J. *et al.* (2005) 'Respiratory correlated cone beam CT', *Medical Physics*. John Wiley and Sons Ltd, 32(4), pp. 1176–1186. doi: 10.1118/1.1869074.

Staub, D. *et al.* (2011) '4D Cone-beam CT reconstruction using a motion model based on principal component analysis', *Medical Physics*. John Wiley and Sons Ltd, 38(12), pp. 6697–6709. doi: 10.1118/1.3662895.

Vedam, S. S. *et al.* (2003) 'Acquiring a four-dimensional computed tomography dataset using an external respiratory signal', *Physics in Medicine and Biology*. IOP Publishing, pp. 45–62. doi: 10.1088/0031-9155/48/1/304.

Wang, J. and Gu, X. (2013) 'Simultaneous motion estimation and image reconstruction (SMEIR) for 4D cone-beam CT.', *Medical physics*, 40(10), p. 101912. doi: 10.1118/1.4821099.

Whelan, B. *et al.* (2017) 'An MRI-compatible patient rotation system - Design, construction, and first organ deformation results':, *Medical Physics*. Wiley Blackwell, 44(2), pp. 581–588. doi: 10.1002/mp.12065.

Whelan, B. *et al.* (2018) 'Patient reported outcomes of slow, single arc rotation: Do we need rotating gantries?', *Journal of Medical Imaging and Radiation Oncology*. John Wiley & Sons, Ltd (10.1111), 62(4), pp. 553–561. doi: 10.1111/1754-9485.12688.

Yang, J. *et al.* (2014) 'Advantages of simulating thoracic cancer patients in an upright position', *Practical Radiation Oncology*. Elsevier, 4(1), pp. e53–e58. doi: 10.1016/j.prro.2013.04.005.

Zhang, Y. *et al.* (2013) 'A technique for estimating 4D-CBCT using prior knowledge and Limited-angle projections', *Medical Physics*. John Wiley and Sons Ltd, 40(12). doi: 10.1118/1.4825097.

Zhi, S., Kachelrieß, M. and Mou, X. (2020) 'High-quality initial image-guided 4D CBCT reconstruction', *Medical Physics*. John Wiley and Sons Ltd., 47(5), pp. 2099–2115. doi: 10.1002/mp.14060.